Analyst

PAPER

View Article Online
View Journal | View Issue

Cite this: *Analyst*, 2019, **144**, 2138

Characterization of CD133$^+$/CD44$^+$ human prostate cancer stem cells with ATR-FTIR spectroscopy

Günnur Güler, *[a,b] Ummu Guven [c] and Gulperi Oktem *[c,d]

Received 15th January 2019,
Accepted 29th January 2019

DOI: 10.1039/c9an00093c

rsc.li/analyst

Current cancer treatments destroy the tumor mass but cannot prevent the recurrence of cancer. The heterogeneous structure of the tumor mass includes cancer stem cells that are responsible for tumor relapse, treatment resistance, invasion and metastasis. The biology of these cells is still not fully understood; therefore, effective treatments cannot be developed sufficiently. Herein, attenuated total reflection-Fourier transform infrared (ATR-FTIR) spectroscopy, combined with unsupervised multivariate analysis, was applied to prostate cancer stem cells (CSCs), non-stem cancer cells (non-CSCs) and normal prostate epithelial cells to elucidate the molecular mechanisms and features of CSCs, which are crucial to improving the target specific therapies. This work revealed the spectral differences in the cellular mechanisms and biochemical structures among three different cell types. Particularly, prostate CSCs exhibit differences in the lipid composition and dynamics when compared to other cell types. CSCs also harbor pronounced differences in their major cellular macromolecules, including differences in the protein amount and content (mainly α-helices), the abundance of nucleic acids (DNA/RNA), altered nucleic acid conformation and carbohydrate composition. Interestingly, macromolecules containing the C=O groups and negatively charged molecules having the COO^- groups are abundant in prostate CSCs in comparison to prostate non-CSCs and normal prostate cells. Overall, this study demonstrates the potential use of ATR-FTIR spectroscopy as a powerful tool to obtain new insights into the understanding of the CSC features, which may provide new strategies for cancer treatment by selectively targeting the CSCs.

Introduction

Most cancer-related deaths are due to drug resistance and metastasis.[1] The war on cancer has been going on for decades, and although cancer treatment continues to improve, cancer is still the leading cause of death. Prostate cancer is ranked at the top in cancer-related deaths among males worldwide.[2] In the prostate cancer cases, resistance to the loss of androgen and chemotherapy continue to be major reasons for therapy failure and death.[3,4] Cancer cells can multiply rapidly and can be resistant to aggressive treatments. The stem cell feature of cancer cells is a key point for cancer progression and in the vast majority of incidences, it is the origin of cancer recurrence.[5–7] While the minor population of cells in a tumor have the capability of self-renewal and the capacity to differentiate, the rest of the tumor cells are non-tumorigenic and are characterized by restricted self-renewal ability.[8,9]

This minor population of tumor cells is 'stem cell-like cells' also termed 'cancer stem cells' (CSCs). CSCs lead to relapse, chemotherapy/radiotherapy resistance, tumorigenesis, progression and invasion.[10–12] They present notable regulatory capacities, such as coordinating cooperation with neighbours to provide nutrients and creating suitable conditions for tumor development. Cancer stem cells are conducive to heterogeneous cell populations that have a high threshold for stress tolerance, high plasticity potential in the tumor microenvironment[13–15] and quiescence as a conventional reaction.[16–19] Due to these specific features, chemotherapy can lead to progression-free survival but does not treat the cancer. Understanding these systems and the structures of cancer stem cells is crucial for the improvement of the target-specific therapies.

CSCs have been isolated on the basis of cell surface markers in many types of cancer such as brain, stomach, lung,

[a]*Center for Drug Research & Development and Pharmacokinetic Applications (ARGEFAR), Ege University, 35100 Izmir, Turkey. E-mail: gunnurgorucu@gmail.com; Tel: +90 232 390 4171, +90 232 750 7700*
[b]*Department of Physics, Science Faculty, Izmir Institute of Technology, 35430 Izmir, Turkey*
[c]*Department of Stem Cell, Ege University Health Science Institute, Izmir, 35100, Turkey. E-mail: goktem@hotmail.com; Tel: +90 232 390 5900*
[d]*Department of Embryology and Histology, School of Medicine, Ege University, 35100 Izmir, Turkey*

breast, colon and prostate cancer.[9,12,20–22] CD133 and CD44 cell surface antigens are the most commonly used biomarkers for isolating and identifying prostate cancer stem cells (PCSCs) by using flow cytometry from prostatic cancer tissue.

Fourier transform infrared (FTIR) spectroscopy uses infrared radiation to cause the molecular bonds within the (bio) sample that absorbs it to vibrate. FTIR provides information on the composition, concentration, dynamics and structure of cellular macromolecules such as lipids, proteins, carbohydrates, nucleic acids, phosphorylated compounds and other metabolites. This powerful technique has been extensively used in a variety of fields for probing cells and other biomedical samples since it is rapid, cost-effective, non-destructive and allows analysis without the requirement of complex sample preparations.[23–28]

Recently, FTIR spectroscopy has been successfully applied to the study of both embryonic and adult stem cell research in a number of ways.[29–35] Spectroscopic characterization of cancer stem cell-like cells from A549 lung carcinoma revealed conformational changes in both proteins and nucleic acids, as well as showed a higher C–O band of carbohydrates in A549 clones enriched with CSCs.[36] Other spectroscopic studies on CSCs in the renal epithelial carcinoma and esophageal adenocarcinoma demonstrated spectral differences in the IR bands associated with lipid, phosphodiester and glycogen.[37,38] Besides, it was reported that the observation of differences between glioblastoma cell fractions with high and low CSC content is associated with the alterations in nucleic acids, carbohydrates and phospholipids.[39] Although synchrotron radiation FTIR (SR-FTIR) has advantages over conventional FTIR spectroscopy, providing a higher signal/noise ratio at the highest spatial resolution due to the high intensity, the conventional FTIR spectroscopic technique has also been successfully applied to the study of cells since it provides a cost-effective, rapid and sensitive analysis. Nevertheless, the determination of the amount of the cells with the attenuated total reflection (ATR) FTIR spectroscopy is challenging because the cells placed on the ATR crystal would most likely be multilayered and overlapping with each other, which might affect the absorbance spectra. The cells should be in good contact with the ATR-crystal to obtain a stable and reproducible spectrum. Based on the aforementioned studies, ATR-FTIR spectroscopy has been widely used in cell biology in terms of basic research and even diagnostic purposes due to the simplicity of sample handling.

The aim of the present study is to identify the differences in the cellular mechanisms and biochemical structures on the molecular level by comparing the prostate cancer stem cells, prostate cancer cells and normal prostate epithelial cells using ATR-FTIR spectroscopy. Unsupervised statistical methods such as principal component analysis (PCA) and hierarchical cluster analysis (HCA), as well as infrared difference spectra and Student's *t*-test, were also applied to the FTIR spectra. Herein, we will reveal the biochemical features of CSCs in prostate cancers, which may provide personalized and effective therapeutic approaches. Biochemical and biophysical characterization of prostate CSCs may also facilitate the understanding of the molecular mechanism of the CSCs and this may help in the finding of new opportunities for anticancer therapy by selectively targeting the CSCs.

Materials and methods

Cell lines

Human prostate cancer cell lines DU-145 were grown in RPMI-1640 (Life Technologies, USA) medium supplemented with 10% FBS (Fetal Bovine Serum) (Life Technologies, USA), 1% penicillin/streptomycin (Life Technologies, USA) and 1% Amphotericin B (Life Technologies, USA). The human prostate epithelial cell line RWPE-1 was grown in Keratinocyte SFM medium (Life Technologies, USA) supplemented with recombinant human Epidermal Growth Factor (rhEGF) and Bovine Pituitary Extract (BPE) (Life Technologies, USA) and maintained in a humidified atmosphere containing 5% CO_2 in an incubator (New Brunswick, UK). Cells were cultured in T-75 flasks (Greiner, USA) and at 80–90% confluence, they were sub-cultured in a 1 : 10 to 1 : 12 split ratio.

Isolation of $CD133^+/CD44^+$ cancer stem cells from the DU-145 cell line

After DU-145 human prostate cancer cells proliferated sufficiently in RPMI-1640 medium (Life Technologies, USA) supplemented with 10% FBS (Life Technologies, USA), 1% penicillin/streptomycin (Life Technologies, USA) and 1% Amphotericin B (Life Technologies, USA), the cells were detached from the flask by using 0.05% Trypsin-EDTA (Life Technologies, USA) and centrifuged at 1000 rpm × 10 min. The cell count and viability were determined using a Muse Cell Analyzer (Millipore, USA) and Cell Count & Viability Kit (MCH100102, Millipore, USA). After the number of cells was determined, the cells were resuspended in an appropriate volume of flow cytometry staining buffer (Beckton Dickinson, USA) so that the final cell concentration was 10×10^6 cell ml^{-1}. The samples were then labelled with CD133-PE (Miltenyi Biotec, UK) (for 10 μL/10^6 cells) and CD44-APC (Miltenyi Biotec, UK) (for 10 μL/10^6 cells) and incubated at 4 °C in the dark for 20 min. After the incubation period was over, the cells were centrifuged at 1000 rpm for 10 min and resuspended with phosphate buffer saline (PBS) (Life Technologies, USA). Finally, the cells were sorted as the $CD133^+/CD44^+$ population (cancer stem cells) and the non-sorting counterparts using the FACS Aria II fluorescence-activated cell sorter. After the isolation process, 1×10^6 cells were obtained. In the analysis performed after the cell sorting, the purity of the $CD133^+/CD44^+$ cancer stem cells was determined to be 88% and the viability of cells 97%.

Hematoxylin and eosin staining protocol

RWPE-1, DU145 $CD133^+/CD44^+$ CSCs and DU-145 non-sorting cells were seeded in 6-well plates at a density of 1×10^5 cells per well. After the cells were attached, the cells were rinsed

twice with cold PBS to remove the medium. Then, 4% paraformaldehyde was added to each well and the plate was stored at +4 °C for 15 min for cell fixation. Following washing with PBS three times, Mayer's hematoxylin (Sigma-Aldrich, USA) was added to each well for 2 min. After washing with tap water and distilled water, eosin (Sigma-Aldrich, USA) was added to each well for 1 min. After washing with PBS three times, the cells were visualized using an Olympus BX 51 (Olympus, Japan).

Preparation of cell suspensions for ATR-FTIR measurements

RWPE-1, DU145 $CD133^+/CD44^+$ CSCs and DU-145 non-sorting cells were resuspended in 1 mL PBS (Life Technologies, USA) for washing and were centrifuged (1000 rpm × 10 min) three times. After removing the supernatant, the cells were resuspended in the sterile physiological NaCl solution with a final concentration of about 1×10^6 cell per mL. Three independent cultures of three types of cells were grown, as given below:

- RWPE-1: Normal human prostate epithelial cells (normal cells)
- DU-145 sorted cells (sort +): Cancer stem cells (CSCs)
- DU-145 non-sorting cells (sort −): Non-stem cancer cells (non-CSCs)

ATR-FTIR spectroscopic measurements

The FTIR measurements were performed with an IRTracer-100 FTIR spectrometer (Shimadzu, Japan) combined with an attenuated total reflection (ATR) unit and equipped with a DLATGS detector. The cell suspension (1.5 μL; about 1×10^6 cells per mL) was deposited on the diamond crystal surface (single-reflection sampling plate) and dried at room temperature for ~12 min under dry air purge conditions to remove the excess water before measurements. To control the dehydration state of the sample and to obtain similar and reproducible spectra, drying of the sample on the ATR plate was followed by monitoring the OH stretching band (4000–3000 cm^{-1}) in the spectrum. A minimum of five spectra per measurement were recorded in the range of 4000–800 cm^{-1} at RT. Three samples taken from each cell type were measured so that the measurements were in triplicate (3 cultures, 3 samples per culture, at least 5 spectra per sample gives at least 15 spectra per cell type); 128 scans were averaged for each interferogram at 4 cm^{-1} spectral resolution. The air spectrum was recorded as background when the ATR plate was empty.

FTIR data processing

Spectral preprocessing, principal component analysis (PCA), difference spectra and Student's *t*-tests were carried out using software Kinetics (provided kindly by Prof. Dr Erik Goormaghtigh from Université libre de Bruxelles, Belgium) running under MATLAB as described previously.[40–42]

Spectral preprocessing. The FTIR spectra were recorded with the spectrometer software program LabSolutions (Shimadzu, Japan). Spectral preprocessing and visualization were performed employing the software Kinetics as follows: atmospheric water vapor contribution in the spectra was subtracted by taking the 1562–1555 cm^{-1} peak as the reference peak, as described previously.[40–43] After the straight lines were interpolated between the selected interval of frequencies (3999, 3970, 3700, 2800, 2700, 1800, 1770, 1480, 1350, 1300, 1145, 1001, 950, 887 and 800 cm^{-1}), they were subtracted from the spectrum for baseline-correction (Rubberband method). Afterwards, the FTIR absorbance spectra were normalized to the equal area between 1582 and 1482 cm^{-1} underneath the amide II band since the amide II area is largely not dependent on the protein secondary structure and less dependent on small variations in the hydration level. Thus, the absorbance scale represents rescaled absorbance values. In the text, "normalized absorbance" refers to 'area-normalized absorbance' that has equal area underneath the amide II band for all FTIR spectra of each type of cell.

Infrared difference spectra and Student's *t*-test. At least 15 spectra (baseline corrected and normalized) collected in triplicate for each cell type (grown independently) were averaged. The average spectra of these triplicates, termed as 'mean' in the current work, were used in the calculation of difference spectra. For instance, the mean absorbance spectrum of 'Cell 1' was subtracted from the absorbance spectrum of 'Cell 2', represented as follows: ΔA = (cell 2)-*minus*-(cell 1). Student's *t*-test was employed at every wavenumber, allowing a statistical comparison between the spectra of each cell type. Herein, the ticker points demonstrate the standard deviations at wavenumbers where a significant difference occurs (with a significance $\alpha = 0.1\%$).

Principal component analysis (PCA). PCA is an unsupervised method used for data reduction, particularly in the analysis of biological samples. It represents the clustering of similar spectra within the data sets in score plots based on the spectral similarities and differences and provides the determination of spectral variables in loading plots (negative and positive loadings).[44] In the present study, PCA was performed for all the spectra of each condition. It was carried out using the fully preprocessed absorbance spectra for the combined spectral range of 3100–2800 and 1800–800 cm^{-1}.

Hierarchical classification. Fully preprocessed (baseline-corrected and normalized) absorbance spectra of the prostate CSCs, prostate cancer cells and normal prostate cells in the combined spectral range of 3100–2800 and 1800–800 cm^{-1} were used as inputs for hierarchical cluster analysis using Ward's clustering algorithm and the squared Euclidian distance.[45] Discriminant characteristics among different types of cells being probed were determined with this method. Herein, the FTIR spectra of the cells are grouped based on the spectral similarities according to many variables. The change in variance between the spectra is described by the heterogeneity values. The higher heterogeneity values among the clusters, calculated automatically by the Kinetics program, reflect the higher differences among clusters.

Results and discussion

The DU145 cell lines were stained with fluorescent conjugated primary antibodies, and prostate cancer stem cells were identi-

fied by the CD133 and CD44 surface markers by using the fluorescence activated cell-sorting method (Fig. 1). Flow cytometry analysis showed the presence of a rare CSC population (1%).

Prior to the cell sorting process, the viability of DU145 cell lines was analyzed by using the Muse Cell Analyzer and was found to be 99.0%. After the sorting process, we controlled the viability of two kinds of cell populations, which were collected and found to be 97% for $CD133^+/CD44^+$ cancer stem cells, 97.1% for non-cancer stem cells. After 1-hour resuspension in NaCl solution, the viability was analyzed again and found to be 94.2% for $CD133^+/CD44^+$ cancer stem cells and 95.1% for non-cancer stem cells. The viability of RWPE-1 cell lines was controlled after the cells were detached and found to be 99.1%, and after 1-hour resuspension in NaCl, the viability was found as 91.1% (Fig. 2).

Fig. 3 displays the phase-contrast microscopy and light microscopy images of the $CD133^+/CD44^+$ prostate cancer stem cells (A–B), non-cancer stem cells (C–D) and RWPE-1 prostate epithelial cells (E–F), respectively. Cells were seeded onto cover glasses for staining protocol. The nucleus/cytoplasm ratio (N : C) is important to detect the maturity of cells. Maturation reduces the N : C ratio. Embryonic and pluripotent stem cells have a higher N : C ratio as compared to other cells. In addition, cancer stem cells have a higher nucleus/cytoplasm ratio than the normal cells. Herein, $CD133^+/CD44^+$ cancer stem cells have a higher N : C ratio (Fig. 3B) than both non-cancer stem cells (Fig. 3D) and RWPE-1 cells (Fig. 3F).

FTIR spectral features of prostate CSCs, non-CSCs and normal prostate cells

Fig. 4 displays the mean absorbance spectra of prostate cancer stem cells (CSCs), prostate cancer cells (non-CSCs) and normal prostate cells recorded in the mid-IR spectral region of 4000–800 cm^{-1}. Molecular vibrations of major cellular macromolecules exhibit characteristic absorption bands in this region. Precisely, the spectral region of 3000–2800 cm^{-1} dominated by lipids originates from the stretching vibrations of the CH groups. The amide I (1700–1600 cm^{-1}) and amide II (1600–1500 cm^{-1}) bands arise mainly from protein secondary structures. The spectral region below 1250 cm^{-1} is dominated by the phosphate groups of nucleic acids and phospholipids as well as by the COH and CC groups of carbohydrates/polysaccharides (for band assignments see ref. 24, 25 and 46–48). In the present work, all spectra were normalized for the equal area in the amide II band as described in the Material and methods section to keep the protein concentration constant so that the spectral variations can be compared relative to the protein concentration.

Fig. 5 represents the lipid C–H stretching region (3000–2800 cm^{-1}) of probed cell lines, originating mainly from the stretching vibrations of CH_3 and CH_2 groups in lipid acyl chains, which can reflect the physical properties of the cell membranes and lipid composition. Obviously, the relative intensity of lipids is lowest in CSCs and highest in the case of normal prostate cells, suggesting that the lipid composition is different among CSCs, non-CSCs and normal prostate cells. The observation of the decreased intensities for the CH_2 bands implies that CSCs exhibit a lower lipid-to-protein ratio. The band broadening and frequency shifting for the lipid CH region provide valuable information about dynamics and order/disorder states of the membrane lipids.[47,49] In CSCs, the band positions of both antisymmetric and symmetric modes of the CH_3 and CH_2 groups slightly broaden (data not shown) and slightly shift towards higher wavenumbers (Fig. 5) in comparison to non-CSCs, reflecting an increased disordering of lipid acyl chains as well as membrane fluidity in CSCs. This sequence of data strongly implies an increased level of cellular network and thus the metastatic behavior of CSCs. In line with our results, the involvement of CSCs in metastasis was reported.[50] A high level of membrane fluidity correlates well with EMT (epithelial to mesenchymal transition), metastatic ability and invasive potential. Researchers showed that inhibition of the CerS6 (ceramide synthase isoform 6) expression decreases the metastatic potential.[51] Also, a recent study reported that breast cancer metastatic capacity can be suppressed by reducing the membrane fluidity.[52] Thus, targeting the cancer stem cell membrane fluidity with developing specific molecules is a highly promising therapeutic approach.

Infrared difference spectra and Student's *t*-test

Fig. 6A displays the FTIR-difference spectra obtained from the mean absorbance spectra shown in Fig. 4. Thicker lines demonstrate the significant differences in absorbance calculated by the Student's *t*-test (α = 0.1%). Herein, each difference

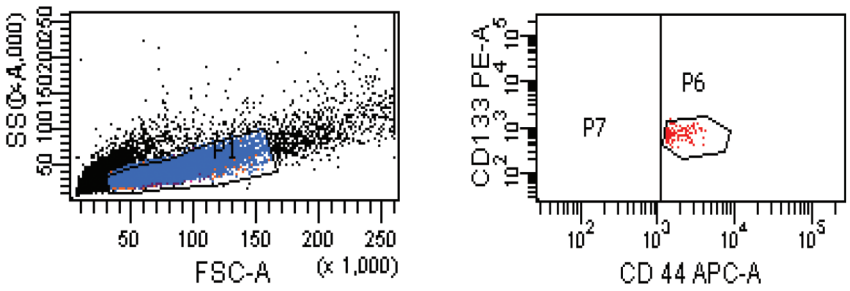

Fig. 1 Isolation charts of $CD133^+/CD44^+$ cancer stem cells enriched from the DU-145 cell lines. The P6 population presents the $CD133^+/CD44^+$ cancer stem cells. SSC, side scatter; FSC, forward scatter.

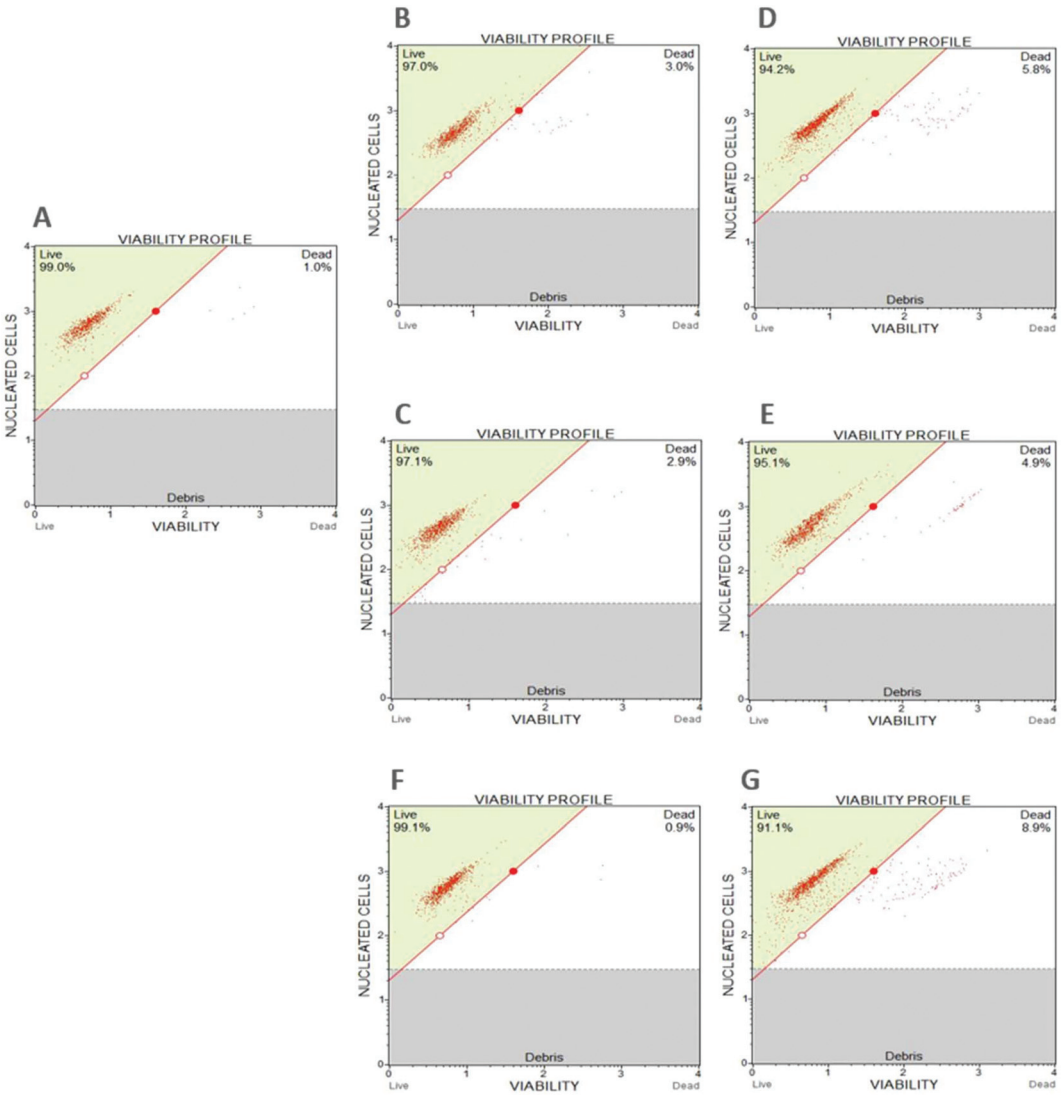

Fig. 2 The viability of cells. Before the cell sorting process, the viability of the DU145 cell line was 99.0% (A). After the sorting process, the viabilities of the $CD133^+/CD44^+$ cancer stem cells were 97% (B) and 97.1% for non-cancer stem cells (C). After 1-hour resuspension in NaCl, the viability was 94.2% for $CD133^+/CD44^+$ cancer stem cells (D) and 95.1% for non-cancer stem cells (E). The viability of the RWPE-1 cell line was 99.1% after the cells were detached (F) and 91.1% after 1-hour resuspension in NaCl (G).

spectrum is sensitive to subtle variations in the band intensity and positions among the probed cell lines, indicating differences in the composition, conformation and/or concentration of cellular macromolecules. A point-by-point description of these difference spectra calculated for (CSCs)-*minus*-(non-CSCs), (CSCs)-*minus*-(normal cells) and for (non-CSCs)-*minus*-(normal cells) is revealed in the following.

Differences between prostate non-stem cancer cells (non-CSCs) and normal prostate cells. In Fig. 6B, the mean absorbance spectrum of normal prostate cells was subtracted from the mean absorbance spectrum of non-CSCs, depicted as (non-CSCs)-*minus*-(normal cells). Herein, the positive peaks represent a high content of the molecular groups in non-CSCs. The positive peaks absorbing at 1686, 1631 and 1537 cm^{-1} were observed in the amide I and II regions attributed to the protein β-sheet structures.[48,53] This clearly indicates that non-CSCs involve a large amount of protein structures rich in β-sheet structures in comparison to the normal prostate cells. Besides, the simultaneous positive peaks were detected at around 1603–1588 and around 1390 cm^{-1}, attributed to the antisymmetric and symmetric stretching vibrations of the COO^- groups, respectively.[54,55] Since these signals are very broad, these peaks are presumably comprised of several COO^- groups. An increase in the peak intensities around 1603 and 1520–1500 cm^{-1} in non-CSCs reflects an increment in the (C–C) stretching vibrations. Significantly, broad and strong bands at around 1217 and 1081 cm^{-1} exist in non-CSCs due to antisymmetric and symmetric stretching vibrations of phosphate groups, respectively.[24,56] In particular, the IR signal of the antisymmetric PO_2^- stretching band at approximately

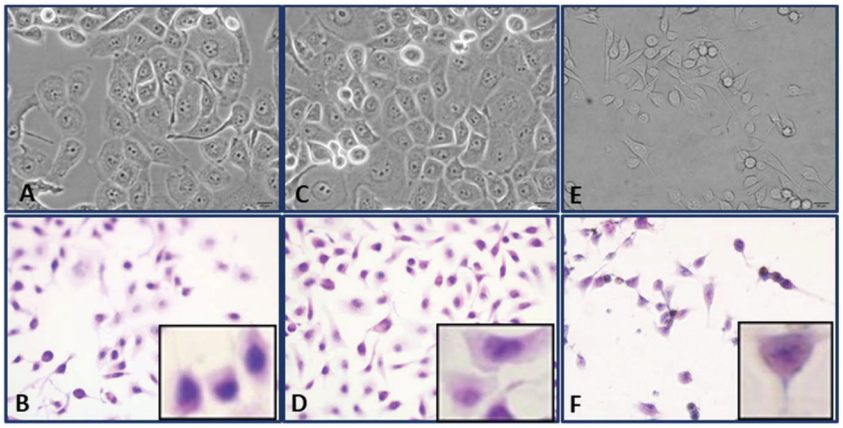

Fig. 3 Phase-contrast microscopy imaging and hematoxylin–eosin staining of $CD133^{+}/CD44^{+}$ cancer stem cells (A–B), non-cancer stem cells (C–D) isolated from the DU145 cell lines and RWPE-1 prostate epithelial cells (E–F) (20× magnification scale bar 50 μm, 40× magnification scale bar 100 μm).

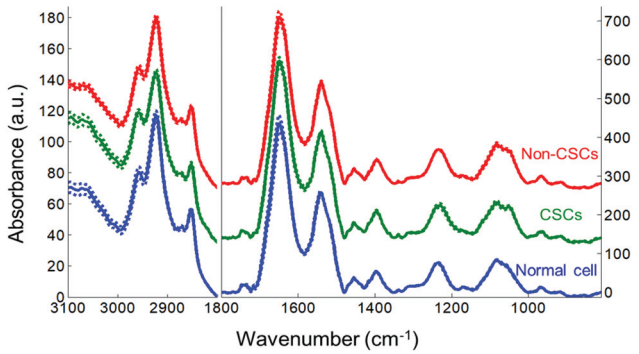

Fig. 4 The FTIR mean absorbance spectra for prostate cancer stem cells (CSCs), prostate cancer cells (non-CSCs) and normal prostate cells (RWPE-1 prostate epithelial cells). The FTIR mean spectra with standard deviations represent the spectral regions of 3100–2800 cm^{-1} and 1800–800 cm^{-1}. The values for the absorbance scale are in absorbance units (a.u). All spectra were rescaled by normalizing the absorbance spectra based on the amide II band area; thus, the absorbance scale represents rescaled absorbance values.

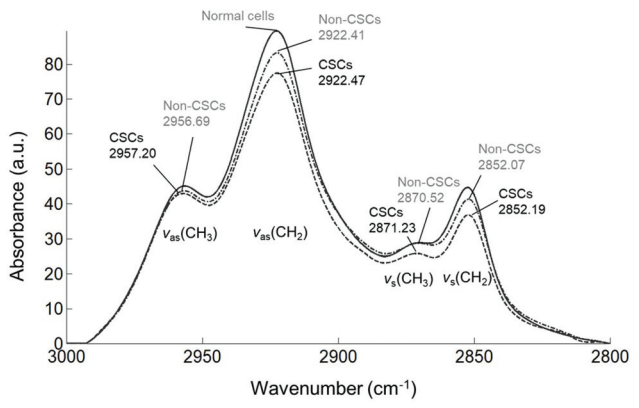

Fig. 5 The mean FTIR absorbance spectra of prostate CSCs (dash line), non-CSCs (dash-dotted line) and normal prostate cells (solid line) representing the lipid CH stretching region.

1217 cm^{-1} is attributed to the Z-helical forms of DNA as a marker for nucleic acid backbone conformation.[57] These IR signals of phosphodiester vibrations cannot arise from the phospholipids since lipid CH peaks at 3000–2800 cm^{-1} as well as lipid ester C=O peaks at 1745 cm^{-1} have negative values in non-CSCs. This strongly shows that the lipid level is significantly lower but nucleic acids are abundant in non-CSCs when compared to the normal prostate cells. This result was also proved by observation of the positive peaks at 1124 cm^{-1} (RNA ribose), 993 cm^{-1} (uracil ring) and at 967 cm^{-1} (phosphodiester vibrations of DNA and RNA) as well as at 1613 and 1707 cm^{-1} (C=O base pair vibrations) (for band assignments see ref. 24, 56 and 58). This suggests that non-CSCs involve high levels of both RNA (less high) and DNA. In fact, IR signals of nucleic acid bases are very weak with respect to protein signals. However, as seen in Fig. 6B, the phosphodiester vibrations are uncommonly high in comparison to protein amide I and II bands. Thus, the positive peaks due to vibrations of the nucleic acid bases were also detected between 1715 and 1500 cm^{-1}. The observation of multiple negative and positive peaks below 1000 cm^{-1} indicates the presence of strong differences in the N-type sugar conformations of the nucleic acid backbone[56,57] between the normal prostate cells and non-CSCs. This altogether indicates that the contents of nucleic acids (both DNA and RNA) increase and DNA molecules undergo alterations in their backbone conformation in the case of non-CSCs when compared to the normal prostate cells. Additionally, strong and broad positive peaks were detected between 1150 and 1000 cm^{-1} in non-CSCs, which can arise from the C–O, C–OH and C–C vibrations of carbohydrates/polysaccharides.[24,46] In this range, differences in the band intensities at around 1144, 1097 and at 1047 cm^{-1} reflect alterations in both the content of carbohydrate derivatives and glycosidic bonds in non-CSCs.

Based on the IR-difference spectrum, non-stem cancer cells harbor a high content of proteins involving β-sheet structures, an increased amount of both DNA and RNA (less high) in con-

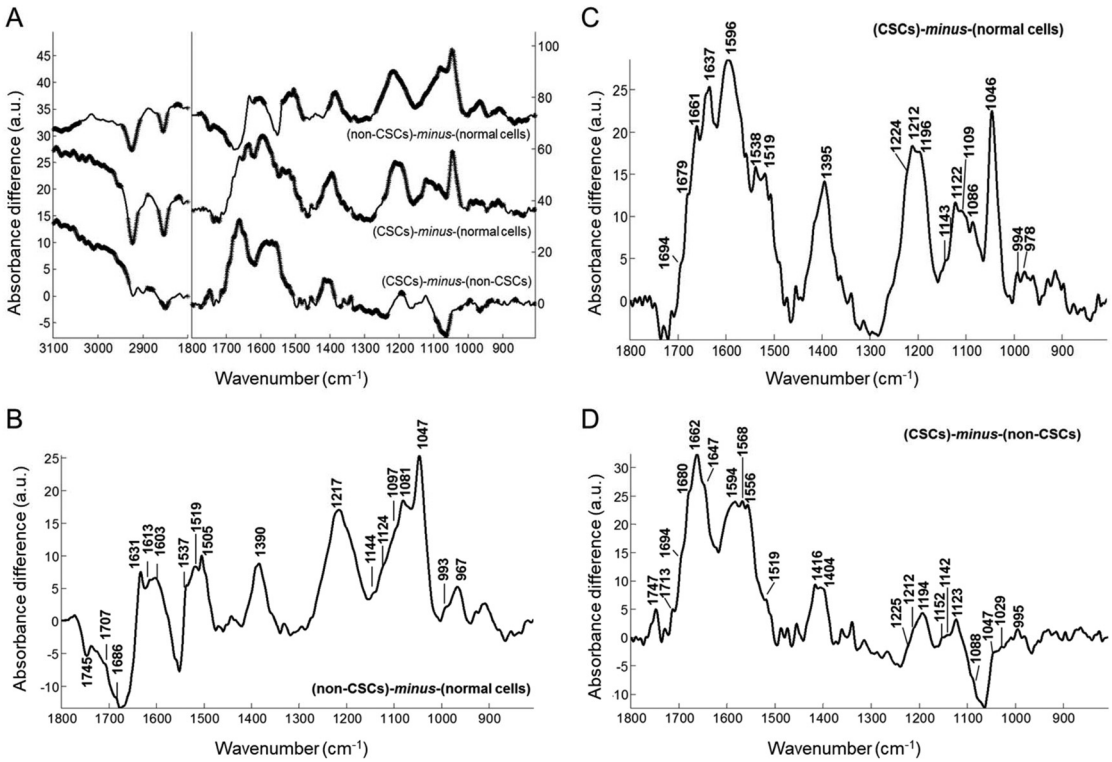

Fig. 6 The FTIR-difference spectra and Student's *t*-test. (A) The difference spectra between the mean spectra of prostate cancer stem cells (CSCs), prostate cancer cells (non-CSCs) and normal prostate cells. Prior to subtraction, the spectra were baseline corrected and normalized to the same area underneath the amide II band. A Student's *t*-test was computed at every wavenumber with a significance level of α = 0.1%. Thicker black lines indicate statistically significant differences between the means. (B, C, D) Closer views of the difference spectra shown in (A) for the region of 1800–800 cm^{-1}.

junction with altered DNA conformation and a high level of carbohydrates/polysaccharides, but have a low content of lipid structures in comparison to the normal prostate cells.

Differences between prostate cancer stem cells (CSCs) and normal prostate cells. The difference spectrum of (CSCs)-*minus*-(normal cells) was calculated by subtraction of the mean absorbance spectrum of normal prostate cells from the mean absorbance spectrum of CSCs (Fig. 6C). CSCs have a dramatically low content of lipid molecules, deduced from the negative absorbance values between 3000–2800 cm^{-1} (CH_2 and CH_3 groups of lipid acyl chains) (Fig. 6A) and at 1715–1750 cm^{-1} (C═O groups of lipid esters), while the amide I and II bands were intensified (Fig. 6C). This indicates that a lower lipid-to-protein ratio was detected in CSCs. Multiple positive peaks at 1694 and 1637 cm^{-1} (β-sheets), 1679 (turn/loop) and at 1661 cm^{-1} (α-helix) were observed in the amide I region, indicating a rise in the protein content in CSCs. The concurrent positive peaks absorbing at 1596–1570 cm^{-1} and 1415–1394 cm^{-1} due to the antisymmetric and symmetric stretching vibrations of the COO^- groups, respectively, were also observed, indicating an increment in the negatively charged molecules in CSCs in comparison to normal prostate cells. Moreover, strong positive bands were detected at around 1224, 1212, 1196 and 1086 cm^{-1} in CSCs, due to the phosphodiester vibrations of nucleic acids. These IR bands were accompanied by an increase in the intensities at 1122 cm^{-1} (RNA ribose), 994 cm^{-1} (uracil ring) and at 978 cm^{-1} (phosphodiester vibrations of DNA and RNA). This shows that nucleic acids (both DNA and RNA) are abundant in CSCs. Besides, significant alterations in the N-type sugar conformations of nucleic acid backbone were observed in CSCs, deduced from the multiple negative and positive peaks below 1000 cm^{-1}. Moreover, pronounced positive peaks were detected between 1160 and 1000 cm^{-1} in CSCs due to carbohydrates/polysaccharides. Differences in the band intensities at around 1143, 1109 and 1046 cm^{-1} reflect some changes in both the content of carbohydrate derivatives and glycosidic bonds in CSCs.

To sum up, in comparison to normal prostate cells, cancer stem cells contain less lipids relative to proteins. The amount, structure and composition of proteins are dramatically different in CSCs, which consist of both α-helical and β-sheet secondary structures. The high levels of both DNA and RNA, altered DNA conformation as well as a high content of carbohydrates/polysaccharides were also observed in CSCs. Macromolecules containing the COO^- groups are strongly abundant in CSCs in comparison to the normal prostate cells.

Differences between prostate cancer stem cells (CSCs) and prostate cancer cells (non-CSCs). The difference spectrum of (CSCs)-*minus*-(non-CSCs) was calculated by subtraction of the

mean absorbance spectrum of prostate cancer cells that are not stem cells (non-CSCs) from the mean absorbance spectrum of prostate cancer stem cells (CSCs), and was shown in Fig. 6A and D. Therein, the positive absorbance reflects the high content of the molecular groups in CSCs with respect to non-CSCs. Absorbance values of the lipid CH_2 and CH_3 groups are slightly lower in CSCs, represented by the negative peaks at 3000–2800 cm^{-1} (Fig. 6A). The signals in this region were associated with the acyl chains existing mainly in lipids. This implies that the lipid amount/composition is different between CSCs and non-CSCs. Besides, the positive signals at 1747 (highest) and 1713 cm^{-1} (C═O vibrations) are quite high in CSCs, which might arise from amino acids and/or other molecular groups containing the C═O groups. The signals in the amide I and II regions, which reflect the protein secondary structures, intensified in CSCs. The observation of intense peaks at 1694 cm^{-1} (β-sheets), 1680 (turn/loop), 1647 (α-helix/unordered) and the highest signal at 1662 cm^{-1} (α-helix) strongly indicate an increased amount of proteins rich in α-helices in the case of CSCs. Simultaneous positive broad bands at 1594–1560 cm^{-1} and 1420–1390 cm^{-1} (COO^- groups) were observed in CSCs, indicating an increment in the negatively charged molecules (a few groups) in comparison to non-CSCs.

Nucleic acid differences are small between CSCs and non-CSCs, deduced from the observation of the weak positive shoulders absorbing at 1225, 1212, 1088 cm^{-1} and the peak at 1194 cm^{-1} due to the phosphodiester vibrations. These peaks cannot be due to phospholipids since the signals of lipid acyl chains were detected as low. However, intense spectral differences could be seen at 1123 and 995 cm^{-1} due most likely to the RNA ribose and uracil ring. These suggest an increase in the content of both RNA (higher) and DNA in CSCs. Similarly, alterations in the N-type sugar conformations of nucleic acid backbone were also observed in CSCs, deduced from the intensity differences below 1000 cm^{-1}. The C–OH vibrations of amino acid side chains such as serine, threonine and tyrosine involved in the phosphorylated proteins and/or other phosphorylated molecules can also contribute to a strong peak around 1194 cm^{-1} in CSCs since the band position is sensitive to the H-bonding.[32,55] The simultaneous observation of the positive peaks at around 1594 and 1520–1500 cm^{-1} in CSCs reflects an increase in the (C–C) stretching vibrations, which might arise from tyrosine and/or other molecular groups (such as carbohydrates) containing the C–C groups.

Other observations were weak positive signals detected at 1152, 1142, 1047 and 1029 cm^{-1} in CSCs, assigned to carbohydrates/polysaccharides. The C–O vibrations of carbohydrate derivatives can also contribute to a strong peak around 1123 cm^{-1} besides RNA. These intensity differences suggest a slight alteration in both the content/composition of carbohydrate derivatives and/or glycosidic bonds in CSCs when compared to the non-CSCs. The C═O and COO^- group signals are quite high in CSCs, suggesting a high content of macromolecules containing the C═O groups and COO^- groups in CSC. Besides, the C–C, C–O and C–OH signals below 1200 cm^{-1} are quite intense in the difference spectrum of CSCs. These altogether suggest that CSCs harbor a high level of carbohydrates/polysaccharides. The differences in the carbohydrates composition between CSCs and non-CSCs are most likely due to having negatively charged polymeric sugars of CSCs. The simultaneous existence of the IR bands corresponding to the high levels of proteins and carbohydrates/polymeric sugars might be due to the abundance of glycoprotein structures in CSCs in comparison to non-CSCs in prostate cancer cells. Differences in carbohydrate content were also observed in several studies done by diverse research groups.[36,59] However, compositional variations in carbohydrates in cells are still not clear.[60]

Based on our FTIR data, observation of an increment in the protein content comprising mainly of α-helical structures in CSCs strongly suggest a higher expression of major gap junction proteins during differentiation. Similar results were also detected in several studies.[29,36] Researchers have shown that an increase in the connexin43 expression, a gap junction protein, is directly linked to high aggressiveness and metastasis. Elevated expression of connexin43 also increased the intravasation and extravasation as it enhanced the gap junctions between the melanoma cells and the endothelial cells. This causes a considerable increase in the metastatic potential.[61] Studies revealed that there is a significant connection between increasing gap junctions and radiotherapy resistance. Enhancement in connexin in the glycoprotein structure and a gap junction component is correlated with radiotherapy resistance in cancer stem cells.[62]

In comparison to prostate non-stem cancer cells (non-CSCs), prostate cancer stem cells (CSCs) involve more lipid molecules. The content and composition of protein structures are pronouncedly different in CSCs, which are rich in the α-helices. Furthermore, an increase in the levels of both RNA (highest) and DNA together with an altered DNA conformation was observed in CSCs. A pronounced difference in the content and composition of carbohydrate derivatives and/or glycosidic bonds between CSCs and non-CSCs was also observed. At most, the content of RNA, proteins and negatively charged molecules are elevated in CSCs, suggesting the increased expression of both protein and RNA molecules accompanied by a rise in the population of negatively charged carbohydrate molecules. This is indicative of the abundance of glycoprotein structures in CSCs when compared to non-CSCs. Phosphorylated molecules may also be abundant in CSCs.

The hierarchical cluster analysis (HCA)

Fig. 7 displays the hierarchical cluster analysis (HCA) performed using all individual absorbance spectra for the combined spectral range of 3100–2800 and 1800–800 cm^{-1} to classify the FTIR spectra of prostate CSCs, non-CSCs and normal cells. It is clear from HCA that these three types of cell lines were successfully discriminated, based on the biochemical variations in lipid, protein, nucleic acid and carbohydrates. Fig. 7 plotted for the spectral range of major cellular macromolecules indicates that the spectra of normal prostate cells

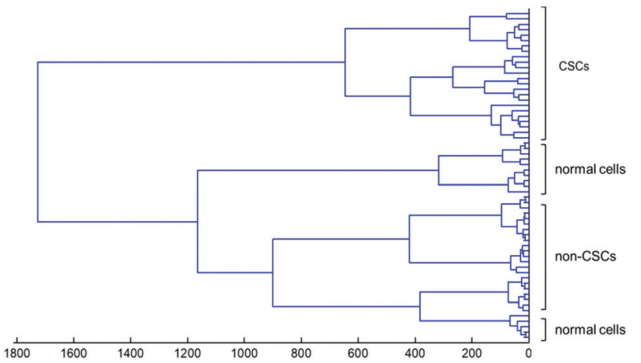

Fig. 7 Hierarchical classification of the individual absorbance spectra for prostate CSCs, non-CSCs and normal prostate cells in the combined spectral ranges of 3100–2800 and 1800–800 cm^{-1}. Classification was based on Euclidean distances between the spectra.

and non-CSCs are clustered together as a first group while all individual spectra of CSCs are grouped separately as a second group, which was distinctly separated from others. Herein, a high heterogeneity value indicates existing of significant biochemical differences among each type of cell lines.

Principal component analysis (PCA)

Fig. 8 displays the PCA score plots presenting the projection of all FTIR spectra in the PC1–PC2 space and the PCA loading plots. PCA, an unsupervised multivariate method, was applied to the absorbance spectra for the combined spectral regions of 3100–2800 and 1800–800 cm^{-1} to reveal the patterns and relationships of the probed cell lines. These three types of cells were effectively distinguished by a mean-centered PCA based on their FTIR spectral features. A PC1 *versus* PC2 plot demonstrates a strong separation of the probed cell lines (Fig. 8A). From PC1, prostate CSCs were clearly separated from both prostate non-CSCs and normal prostate cells for a total of 63.3% while both prostate cancer cells and cancer stem cells were distinguished from the normal prostate cells for a total of 25.7% in PC2. The variability within the clusters observed in the PCA score plots is not due to the sample preparation for the FTIR analysis. In this respect, the viability states of each cell type were analyzed after 1-hour resuspension in NaCl solution (timing for the FTIR analysis of dried cells without chemical fixation). According to the viability assessment (Fig. 2), the viability of the cells was found above 91%, indicating that each cell type has a high population of live cells and was not significantly affected when incubated in the sterile physiological NaCl solution.

The PCA loading plots represent the spectral regions associated with the separation of each clustering in the PCA score plot. According to the PC1 loading plot (Fig. 8B), prostate cancer stem cells have negative peaks at the lipid region (3000–2800 cm^{-1}) but have multiple positive values at 1660 and 1556 cm^{-1} (α-helical proteins) in the amide I and amide II regions, between 1750–1700 cm^{-1} (C═O groups), at 1586, 1570 and a broad band at 1408 cm^{-1} (COO^- groups). Besides, the

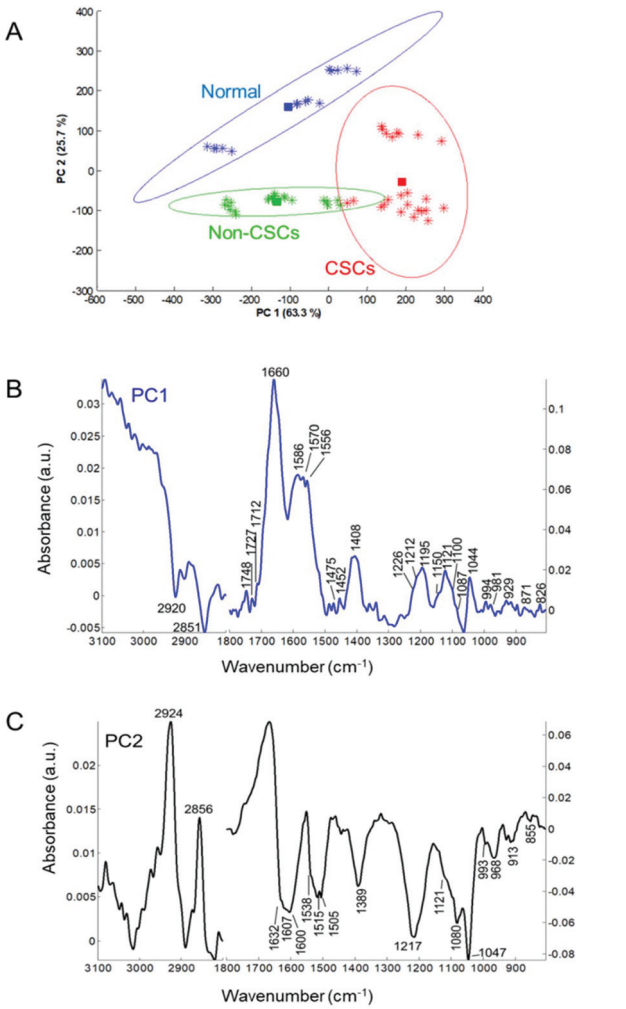

Fig. 8 Principal component analysis. (A) The PCA score plots and (B, C) first two PCA loading plots for all cells. Values in brackets represent the percentage of total variance in each PC. A mean-centered PCA was performed for the combined spectral regions of 3100–2800 and 1800–800 cm^{-1}.

observation of positive peaks below 1300 cm^{-1} corresponds to the phosphate groups and ring vibrations of nucleic acids (both DNA and RNA) as well as C–OH and CO–O–C vibrations of carbohydrates and polymeric sugars. These altogether suggest that prostate CSCs are well distinguished from both prostate non-CSCs and normal prostate cells by a high content of α-helical proteins and the conformation of the protein structures, compositional differences in carbohydrate derivatives and their abundance, a high amount of nucleic acids (both DNA and RNA), a low content of lipids and by altered DNA conformation. The list of peaks obtained in the PC1 and PC2 loadings are summarized in Table 1.

On the other hand, the spectra of both prostate CSCs and non-CSCs are separated from the normal prostate cells by the negative correlation of the PC2 score (Fig. 8C). Both prostate CSCs and non-CSCs have positive peaks in the lipid region (3000–2800 cm^{-1}), while they have negative values for the PC2

Table 1 The IR peaks in the PC1 and PC2 loadings obtained from Fig. 8B and C, and their corresponding band assignments for functional groups. The (+) peaks in the PC1 loading indicate upregulation of the macromolecular components in the prostate CSCs. The (–) peaks in the PC2 loading indicate upregulation of the macromolecular components in the prostate cancer cells (non-CSCs) and prostate cancer stem cells (CSCs). The assignment of the IR spectral bands is based on literature[24,48,53,54] (ν, stretching; δ, bending; as, antisymmetric; s, symmetric)

(+) peaks in the PC1 loading (cm^{-1})	(–) peaks in the PC2 loading (cm^{-1})	Band assignments
1748, 1727	—	Ester ν(C═O)
1660	—	Amide I, α-helices ν(C═O)
—	1632	Amide I, β-sheets ν(C═O)
1586, 1570	1600	$\nu_{as}(COO^{-})$
1556	—	Amide II, α-helices
—	1538	Amide II, β-sheets
1408	1389	$\nu_{s}(COO^{-})$
1226, 1212, 1195	1217	$\nu_{as}(PO_2^{-})$
1121, 1100	1121	ν(C–O), RNA ribose
1087	1080	$\nu_{s}(PO_2^{-})$
1044	1047	ν_{s}(C–O) and δ(C–O): C–OH groups
994	993	C–O ribose, C–C
981	968	$\nu(PO_4^{-})$
929	913	Sugar-phosphate skeletal motions
871, 826	855	Nucleic acid backbone

loading at 1632 and 1538 cm^{-1} (β-sheet protein structures), broad bands both at around 1600 and 1389 cm^{-1} (antisymmetric and symmetric stretching vibrations of COO^{-} groups, respectively), at around 1217 and 1080 cm^{-1} ($\nu_{as}PO_2^{-}$ and $\nu_{s}PO_2^{-}$ of phosphate groups in nucleic acids, respectively), at 1121 and 993 cm^{-1} (RNA ribose), at 1047 cm^{-1} (carbohydrate derivatives), and multiple negative and positive values below 950 cm^{-1} (altered DNA conformation). These altogether indicate that both prostate CSCs and non-CSCs are well separated from the normal prostate cells based on variations in their cellular macromolecules. Significantly, both nucleic acids and carbohydrates are abundant in the case of prostate CSCs and non-CSCs in comparison to normal prostate cells. The PCA results are in accord with the observations in the difference spectra described above (Fig. 6).

Conclusion

ATR-FTIR spectroscopy was employed as a fast, non-destructive and cost-effective experimental technique to investigate and characterize the subpopulation of prostate cancer cells, so-called cancer stem cells (CSCs). FTIR spectral analysis, together with the application of principal component analysis and hierarchical clustering analysis, was used to monitor the differences in the cellular macromolecules of prostate cancer stem cells (CSCs) as compared to the prostate non-stem cancer cells (non-CSCs) and normal prostate epithelial cells.

In the current work, the differences in the lipid structures of the cell types could originate from plasma membrane lipids and/or intracellular lipid drops. CSCs exhibit disordered lipid acyl chains as well as increased membrane fluidity when compared to both non-CSCs and normal cells, suggesting an increased level of cellular network and metastasis in the case of CSCs. The protein amount and composition are harshly different in CSCs that harbor a high level of proteins rich in α-helices. Similarly, the RNA level was the highest in the case of CSCs as compared to the other cell types. This demonstrates an increase in the expression level of both RNA and protein structures, implying increased transcriptional activity. Both CSCs and non-CSCs have an altered nucleic acid conformation, high amounts of DNA and carbohydrates. The simultaneous increase in the levels of both proteins and carbohydrates suggests the abundance of glycoprotein structures in CSCs and non-CSCs when compared to the normal cells, suggesting a change in the metabolic activity and cellular interactions. Similarly, the macromolecules containing the C═O, COO^{-} and C–C groups are abundant in both the CSCs (highest) and non-CSCs, suggesting large differences in the content and composition of carbohydrates and/or glycosidic bonds, probably due to the negatively charged carbohydrate derivatives. These cellular disparities on the molecular level were confirmed by PCA and HCA, which could successfully discriminate the spectra of CSCs from both non-CSCs and normal cells. Observed spectral differences in PCA loadings are the result of biochemical differences among probed cell types. These altogether suggest the existence of significant differences in the lipidemic, genomic, proteomic and metabolic mechanisms of prostate CSCs (largely), non-CSCs and normal prostate cells.

FTIR spectroscopic analysis could discriminate the prostate CSCs from both non-CSCs and normal prostate cells based on the cellular biochemical and biophysical features. Thus, the present work indicates the applicability of ATR-FTIR spectroscopy as a powerful technique to gain new insights into the understanding of the mechanisms in CSCs, which may provide new opportunities for anti-cancer therapy by selectively targeting the CSCs.

Abbreviations

FTIR spectroscopy	Fourier transform infrared spectroscopy
ATR	Attenuated total reflection
DU-145	Human prostate cancer cell line

RWPE-1	Human epithelial cell line
BSA	Bovine serum albumin
BPE	Bovine pituitary extract
CSCs	Cancer stem cells
non-CSCs	Non-stem cancer cells
rhEGF	Recombinant human epidermal growth factor
PCSC	Prostate cancer stem cell
FACS	Fluorescence-activated cell sorting
APC	Allophycocyanin
PE	Phycoerythrin
PBS	Phosphate buffer saline
ν_{as}	Antisymmetric stretching
ν_{s}	Symmetric stretching
δ	Bending vibrations
EMT	Epithelial to mesenchymal transition
CerS6	Ceramide synthase isoform 6

Conflicts of interest

The authors declare no conflict of interest.

Acknowledgements

The authors would like to give special acknowledgment to ARGEFAR, Ege University for providing ATR-FTIR instrumental facility. We also thank Prof. Dr Erik Goormaghtigh from Université Librede Bruxelles, Belgium, for generously providing the software Kinetics.

References

1 C. Chaffer and R. A. Weinberg, *Science*, 2011, **331**, 1559–1564.
2 C. R. Uk, *Cancer Res.*, 2014, **2012**, 2012–2015.
3 J. Ni, P. Cozzi, J. Hao, W. Duan, P. Graham, J. Kearsley and Y. Li, *Curr. Cancer Drug Targets*, 2014, **14**, 225–240.
4 B. Sharpe, M. Beresford, R. Bowen, J. Mitchard and A. D. Chalmers, *Stem Cell Rev. Rep.*, 2013, **9**, 721–730.
5 S. Colak and J. P. Medema, *FEBS J.*, 2014, **281**, 4779–4791.
6 H. O. Kaseb, H. Fohrer-Ting, D. W. Lewis, E. Lagasse and S. M. Gollin, *Exp. Cell Res.*, 2016, **348**, 75–86.
7 C. Gedye, D. Sirskyj, N. C. Lobo, J. Meens, E. Hyatt, M. Robinette, N. Fleshner, R. J. Hamilton, G. Kulkarni, A. Zlotta, A. Evans, A. Finelli, M. A. S. Jewett and L. E. Ailles, *Sci. Rep.*, 2016, **6**, 25220.
8 M. F. Clarke, *Biol. Blood Marrow Transplant.*, 2005, **11**, 14–16.
9 X. Wu, H. Chen and X. Wang, *Cancer Treat. Rev.*, 2012, **38**, 580–588.
10 K. Polyak and W. C. Hahn, *Nat. Med.*, 2006, **12**, 296–300.
11 T. Reya, S. J. Morrison, M. F. Clarke and I. L. Weissman, *Nature*, 2001, **414**, 105–111.
12 S. Takaishi, T. Okumura, S. Tu, S. S. Wang, W. Shibata, R. Vigneshwaran, S. A. Gordon, Y. Shimada and T. C. Wang, *Stem Cells*, 2009, **27**, 1006–1020.
13 J. Wu and J. C. Izpisua Belmonte, *Cell*, 2016, **165**, 1572–1585.
14 N. Moore and S. Lyle, *J. Oncol.*, 2011, **2011**, 396076.
15 C. L. Chaffer, I. Brueckmann, C. Scheel, A. J. Kaestli, P. A. Wiggins, L. O. Rodrigues, M. Brooks, F. Reinhardt, Y. Su, K. Polyak, L. M. Arendt, C. Kuperwasser, B. Bierie and R. A. Weinberg, *Proc. Natl. Acad. Sci. U. S. A.*, 2011, **108**, 7950–7955.
16 M. C. Cabrera, R. E. Hollingsworth and E. M. Hurt, *World J. Stem Cells*, 2015, **7**, 27–36.
17 T. Borovski, F. De Sousa E Melo, L. Vermeulen and J. P. Medema, *Cancer Res.*, 2011, **71**, 634–639.
18 V. Plaks, N. Kong and Z. Werb, *Cell Stem Cell*, 2015, **16**, 225–238.
19 P. M. Aponte and A. Caicedo, *Stem Cells Int.*, 2017, **2017**, 5619472.
20 C. Li, D. G. Heidt, P. Dalerba, C. F. Burant, L. Zhang, V. Adsay, M. Wicha, M. F. Clarke and D. M. Simeone, *Cancer Res.*, 2007, **67**, 1030–1037.
21 M. Al-Hajj and M. F. Clarke, *Oncogene*, 2004, **23**, 7274–7282.
22 G. Farnie and R. B. Clarke, *Stem Cell Rev.*, 2007, **3**, 169–175.
23 K. L. Andrew Chan and S. G. Kazarian, *Chem. Soc. Rev.*, 2016, **45**, 1850–1864.
24 Z. Movasaghi, S. Rehman and I. ur Rehman, *Appl. Spectrosc. Rev.*, 2008, **43**, 134–179.
25 M. Diem, S. Boydston-White and L. Chiriboga, *Appl. Spectrosc.*, 1999, **53**, 148A–161A.
26 G. Bellisola and C. Sorio, *Am. J. Cancer Res.*, 2012, **2**, 1–21.
27 A. Benard, C. Desmedt, M. Smolina, P. Szternfeld, M. Verdonck, G. Rouas, N. Kheddoumi, F. Rothé, D. Larsimont, C. Sotiriou and E. Goormaghtigh, *Analyst*, 2014, **139**, 1044–1056.
28 A. Gaigneaux, C. Decaestecker, I. Camby, T. Mijatovic, R. Kiss, J. Ruysschaert and E. Goormaghtigh, *Exp. Cell Res.*, 2004, **297**, 294–301.
29 D. Ami, T. Neri, A. Natalello, P. Mereghetti, S. M. Doglia, M. Zanoni, M. Zuccotti, S. Garagna and C. A. Redi, *Biochim. Biophys. Acta*, 2008, **1783**, 98–106.
30 P. Heraud, E. S. Ng, S. Caine, Q. C. Yu, C. Hirst, R. Mayberry, A. Bruce, B. R. Wood, D. McNaughton, E. G. Stanley and A. G. Elefanty, *Stem Cell Res.*, 2010, **4**, 140–147.
31 W. Tanthanuch, K. Thumanu, C. Lorthongpanich, R. Parnpai and P. Heraud, *J. Mol. Struct.*, 2010, **967**, 189–195.
32 J. Cao, E. S. Ng, D. McNaughton, E. G. Stanley, A. G. Elefanty, M. J. Tobin and P. Heraud, *Int. J. Mol. Sci.*, 2013, **14**, 17453–17476.
33 C. Aksoy and F. Severcan, *Spectrosc. Int. J.*, 2012, **27**(3), 167–184.
34 G. J. Vazquez-Zapien, M. M. Mata-Miranda, V. Sanchez-Monroy, R. J. Delgado-Macuil, D. G. Perez-Ishiwara and M. Rojas-Lopez, *Stem Cells Int.*, 2016, **2016**, 1–10.

35 G. Güler, E. Acikgoz, N. Ü. Karabay Yavasoglu, B. Bakan, E. Goormaghtigh and H. Aktug, *Analyst*, 2018, **143**, 1624–1634.
36 M. M. S. Balla, R. S. Ningthoujam, M. Kumar, J. R. Bandekar and B. N. Pandey, *J. Cancer Res. Ther.*, 2016, **12**, 1144–1152.
37 C. Hughes, M. Liew, A. Sachdeva, P. Bassan, P. Dumas, C. A. Hart, M. D. Brown, N. W. Clarke and P. Gardner, *Analyst*, 2010, **135**, 3133.
38 R. Zhao, L. Quaroni and A. G. Casson, *Analyst*, 2010, **135**, 53–61.
39 O. Uckermann, R. Galli, M. Anger, C. Herold-Mende, E. Koch, G. Schackert, G. Steiner and M. Kirsch, *Int. J. Radiat. Biol.*, 2014, **90**, 710–717.
40 A. Derenne, M. Verdonck and E. Goormaghtigh, *Analyst*, 2012, **137**, 3255–3264.
41 G. Güler, E. Acikgoz, N. Ü. Karabay Yavasoglu, B. Bakan, E. Goormaghtigh and H. Aktug, *Analyst*, 2018, **143**(7), 1624–1634.
42 A. Derenne, V. Van Hemelryck, D. Lamoral-Theys, R. Kiss and E. Goormaghtigh, *Biochim. Biophys. Acta*, 2013, **1832**, 46–56.
43 E. Goormaghtigh and J. M. Ruysschaert, *Spectrochim. Acta, Part A*, 1994, **50**, 2137–2144.
44 R. A. Johnson and D. W. Wichern, *Principal Components, Applied Multivariate Statistical Analysis*, Prentice Hall, Upper Saddle River, 4th edn, 1998, pp. 458–513.
45 J. H. Ward Jr., *J. Am. Stat. Assoc.*, 1963, **58**, 236–244.
46 M. Kacuráková and M. Mathlouthi, *Carbohydr. Res.*, 1996, **284**, 145–157.
47 G. Güler, R. M. Gärtner, C. Ziegler and W. Mäntele, *J. Biol. Chem.*, 2016, **291**, 4295–4307.
48 H. Fabian and W. Mäntele, in *Handbook of Vibrational Spectroscopy*, ed. J. M. Chalmers and P. R. Griffiths, John Wiley & Sons, Ltd, Chichester, UK, 2006, pp. 3399–3425.
49 F. Korkmaz, S. Köster, Ö. Yildiz and W. Mäntele, *Biochemistry*, 2008, **47**, 12126–12134.
50 H. Li and D. G. Tang, *J. Surg. Oncol.*, 2011, **103**, 558–562.
51 V. Edmond, F. Dufour, G. Poiroux, K. Shoji, M. Malleter, A. Fouqué, S. Tauzin, R. Rimokh, O. Sergent, A. Penna, A. Dupuy, T. Levade, N. Theret, O. Micheau, B. Ségui and P. Legembre, *Oncogene*, 2015, **34**, 996–1005.
52 W. Zhao, S. Prijic, B. C. Urban, M. J. Tisza, Y. Zuo, L. Li, Z. Tan, X. Chen, S. A. Mani and J. T. Chang, *Cancer Res.*, 2016, **76**, 2037–2049.
53 E. Goormaghtigh, V. Cabiaux and J. M. Ruysschaert, in *Subcellular biochemistry*, ed. H. J. Hilderson and G. B. Ralston, Plenum Press, New York and London, 1994, vol. 23, pp. 329–362.
54 G. Güler, E. Džafić, M. M. Vorob'Ev, V. Vogel and W. Mäntele, *Spectrochim. Acta, Part A*, 2011, **79**, 104–111.
55 A. Barth, *Prog. Biophys. Mol. Biol.*, 2000, **74**, 141–173.
56 G. I. Dovbeshko, N. Y. Gridina, E. B. Kruglova and O. P. Pashchuk, *Talanta*, 2000, **53**, 233–246.
57 M. Banyay, M. Sarkar and A. Gräslund, *Biophys. Chem.*, 2003, **104**, 477–488.
58 B. R. Wood, *Chem. Soc. Rev.*, 2016, **45**, 1980–1998.
59 S. O. Konorov, H. G. Schulze, C. G. Atkins, J. M. Piret, S. A. Aparicio, R. F. B. Turner and M. W. Blades, *Anal. Chem.*, 2011, **83**, 6254–6258.
60 H. J. An, P. Gip, J. Kim, S. Wu, K. W. Park, C. T. McVaugh, D. V. Schaffer, C. R. Bertozzi and C. B. Lebrilla, *Mol. Cell. Proteomics*, 2012, **11**(4), M111.010660.
61 M. Saito-Katsuragi, H. Asada, H. Niizeki, F. Katoh, M. Masuzawa, M. Tsutsumi, H. Kuniyasu, A. Ito, H. Nojima and S. Miyagawa, *Cancer*, 2007, **110**, 1162–1172.
62 H. Dertinger and D. Hülser, *Radiat. Environ. Biophys.*, 1981, **19**, 101–107.